IOPscience iopscience.iop.org

Home Search Collections Journals About Contact us My IOPscience

Thermal properties of lateral-current-injection semiconductor membrane Fabry–Perot laser under continuous-wave operation

This content has been downloaded from IOPscience. Please scroll down to see the full text.

2015 Jpn. J. Appl. Phys. 54 042701

(http://iopscience.iop.org/1347-4065/54/4/042701)

View the table of contents for this issue, or go to the journal homepage for more

Download details:

IP Address: 131.112.10.178
This content was downloaded on 19/07/2017 at 17:47

Please note that terms and conditions apply.

You may also be interested in:

Low-threshold-current operation of membrane distributed-feedback laser with surface grating bonded on Si substrate
Yuki Atsuji, Kyohei Doi, Takuo Hiratani et al.

Room-temperature continuous-wave operation of GaInAsP/InP lateral-current-injection membrane laser bonded on Si substrate
Daisuke Inoue, Jieun Lee, Kyohei Doi et al.

Waveguide loss reduction of lateral-current-injection type GaInAsP/InP membrane Fabry–Pérot laser
Takahiro Tomiyasu, Takuo Hiratani, Daisuke Inoue et al.

90 °C continuous-wave operation of GaInAsP/InP membrane distributed-reflector laser on Si substrate
Takuo Hiratani, Daisuke Inoue, Takahiro Tomiyasu et al.

Preliminary reliability test of lateral-current-injection GaInAsP/InP membrane distributed feedback laser on Si substrate fabricated by adhesive wafer bonding
Kai Fukuda, Daisuke Inoue, Takuo Hiratani et al.

High-differential quantum efficiency operation of GaInAsP/InP membrane distributed-reflector laser on Si
Takahiro Tomiyasu, Takuo Hiratani, Daisuke Inoue et al.

Continuous Wave Operation of Thin Film Lateral Current Injection Lasers Grown on Semi-Insulating InP Substrate
Tadashi Okumura, Hitomi Ito, Daisuke Kondo et al.

Room-temperature continuous-wave operation of membrane distributed-reflector laser
Takuo Hiratani, Daisuke Inoue, Takahiro Tomiyasu et al.

Japanese Journal of Applied Physics **54**, 042701 (2015) **REGULAR PAPER**
http://dx.doi.org/10.7567/JJAP.54.042701

Thermal properties of lateral-current-injection semiconductor membrane Fabry–Perot laser under continuous-wave operation

Takuo Hiratani[1*], Kyohei Doi[1], Jieun Lee[1], Daisuke Inoue[1], Tomohiro Amemiya[2], Nobuhiko Nishiyama[1], and Shigehisa Arai[1,2]

[1]*Department of Electrical and Electronic Engineering, Tokyo Institute of Technology, Meguro, Tokyo 152-8550, Japan*
[2]*Quantum Nanoelectronics Research Center, Tokyo Institute of Technology, Meguro, Tokyo 152-8552, Japan*
E-mail: hiratani.t.aa@m.titech.ac.jp

Received November 10, 2014; revised January 6, 2015; accepted January 19, 2015; published online March 6, 2015

For the realization of on-chip optical interconnects, light sources enabling ultralow power consumption and high-efficiency operation are required. With this aim, we fabricated lateral-current-injection-type membrane Fabry–Perot lasers with a threshold current of 3.5 mA and an external differential quantum efficiency of 11% under a room temperature-continuous wave (RT-CW) condition. To the best of our knowledge, we experimentally evaluated the thermal properties of a membrane laser for the first time. From the measurement, we obtained a thermal resistance of 330 K/W, which well agreed with the theoretical value of 340 K/W. From the theoretical analysis, it was found that a reduction of the benzocyclobutene thickness was effective for reducing the thermal resistance of the membrane laser. Finally, we determined that the increase in thermal resistance for short cavity (less than 50 μm) devices is not a problem because self-heating is small for low operation current.
© 2015 The Japan Society of Applied Physics

1. Introduction

The introduction of optical interconnects to LSI circuits can solve problems including the resistor–capacitor (RC) delay or ohmic heating in electrical interconnects.[1–5] These problems have occurred following the scaling of LSI[6] and will limit the performance of LSI. For the realization of on-chip optical interconnects, optical devices with ultralow power-consumption operation, a small footprint, easy integration with other optical components, and highly efficient light output are required. Regarding the light sources, an available energy of 100 fJ/bit was estimated.[7] Recently, vertical-cavity surface-emitting lasers (VCSELs),[8–11] microdisk lasers,[12,13] and photonic crystal (PhC) lasers[14–16] were reported as ultralow-energy light sources.

In order to satisfy these requirements, we proposed semiconductor membrane photonic integrated circuits (PICs) including membrane distributed feedback (DFB) lasers, III–V waveguides, and membrane detectors on a Si platform, as shown in Fig. 1. The membrane structure consists of a thin (typically 150–250 nm) semiconductor core layer sandwiched by top and bottom low-refractive-index cladding materials such as air, SiO_2, and benzocyclobutene (BCB). Because this structure enables an enhancement in the optical confinement factor in the active region by a factor of approximately three compared to conventional edge-emitting lasers, low-threshold-current operation due to the enhanced modal gain is expected. Low-threshold RT-CW operation under the optical pumping of the membrane DFB laser was demonstrated, and the CW operation was obtained, even up to 85 °C.[17–20]

However, it is difficult to inject current vertically because the optical mode field spreads into the top and bottom electrodes, which results in extraordinary absorption. Therefore, we proposed to adopt a lateral-current-injection (LCI) structure to realize an injection-type membrane laser[21] and obtained pulsed operation of the LCI laser prepared on a semi-insulating InP substrate.[22] Then, the LCI structure was introduced to the membrane laser with the help of the BCB bonding technique.[23] Even though a relatively low threshold current of 3.8 mA was obtained under RT pulsed conditions, RT-CW operation could not be obtained owing to the large

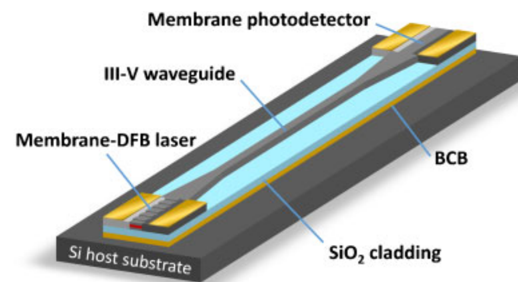

Fig. 1. (Color online) Schematic of the membrane PICs on a Si platform.

thermal resistance of the BCB layer.[24] By reducing the thickness of the BCB layer to reduce the thermal resistance, RT-CW operation of the LCI membrane laser was realized for the first time.[25]

In this paper, to the best of our knowledge, the thermal resistance of the LCI membrane laser is experimentally evaluated for the first time from the peak lasing wavelength shift versus the dissipated electric power, and it is compared with the theoretical result. Further, we formulated an appropriate calculation model for analyzing the thermal resistance by comparing the simulation with experimental results. Finally, we showed that the reduction of BCB thickness is an effective method for reducing the thermal resistance evaluated through experiments and calculations.

2. Design and fabrication process

Figure 2(a) shows a schematic of the LCI membrane Fabry–Perot (FP) laser. The fabrication process of the LCI membrane FP laser begins with an initial wafer consisting of a Be-doped p-GaInAs contact layer and a core layer grown on an n-InP substrate grown by gas-source MBE (GSMBE) [Fig. 3-1)]. The core layer contains a strain-compensated five quantum-well (5QW) structure, which consists of five 1% compressively-strained $Ga_{0.22}In_{0.78}As_{0.81}P_{0.19}$ wells with 0.15% tensile-strained $Ga_{0.26}In_{0.74}As_{0.49}P_{0.51}$ barriers, undoped GaInAsP optical confinement layers (OCLs), and undoped InP cap layers. The total core layer thickness is

 © 2015 The Japan Society of Applied Physics

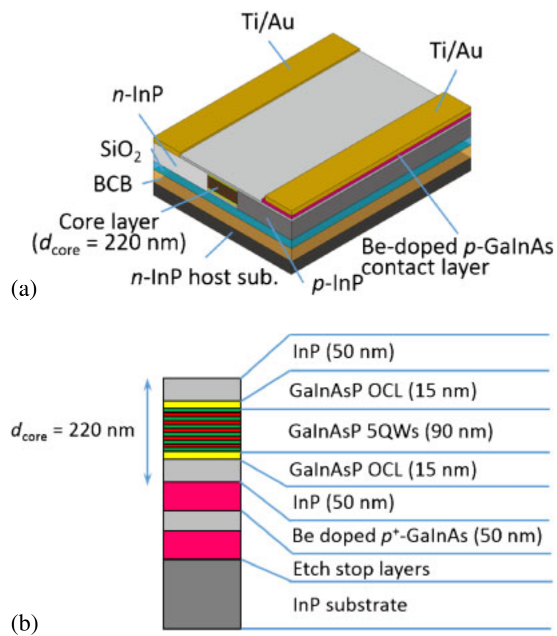

Fig. 2. (Color online) Schematics of the (a) LCI-membrane FP laser and (b) initial wafer structure with a core thickness of 220 nm.

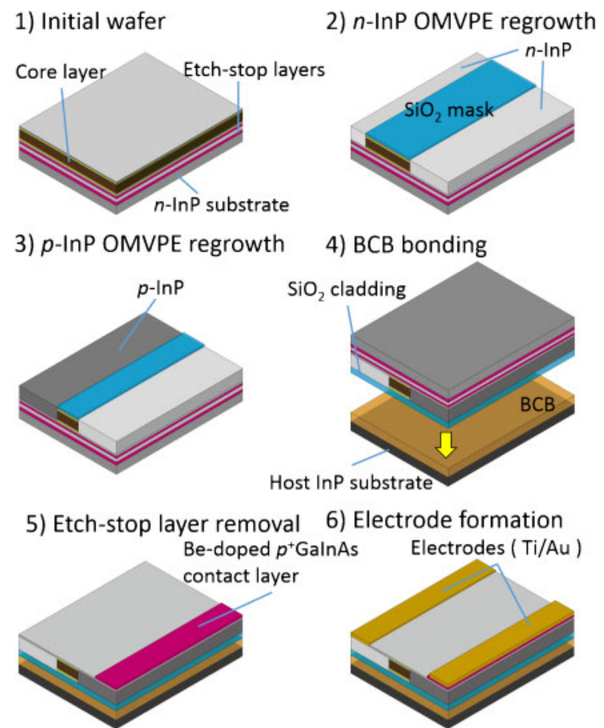

Fig. 3. (Color online) Fabrication process of an LCI-membrane FP laser.

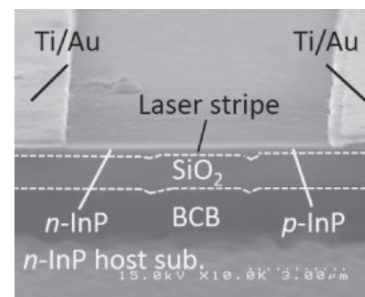

Fig. 4. Cross-sectional SEM image of the fabricated LCI-membrane FP laser.

220 nm, as shown in Fig. 2(b). A Be-doped contact layer was adopted to suppress the diffusion of dopants into the active region. The optical confinement factor is 3.2%/well, which is 1.5 times larger than that of the previously reported device with a core thickness of 470 nm.[24]

First, the LCI structure was formed by two-step organometallic vapor-phase epitaxy (OMVPE) selective-area regrowth. Using photolithography and CH_4/H_2 reactive-ion etching (RIE), 7-μm-wide mesas were formed, and the n-InP (doping concentration $N_D = 4 \times 10^{18}\,cm^{-3}$) layer was regrown at both sides of the mesa with SiO_2 masks [Fig. 3-2)]. Afterwards, the n-InP layer on one side of the mesa and part of the mesa were etched by the same method to form a narrow (1–2 μm) stripe geometry, and the p-InP (doping concentration $N_A = 4 \times 10^{18}\,cm^{-3}$) layer was regrown [Fig. 3-3)].

After preparing the LCI structure, a 1-μm-thick SiO_2 layer was deposited by a plasma-chemical-vapor-deposition system and was BCB bonded to another InP host substrate. A 2-μm-thick layer of BCB was coated onto the InP host substrate, and the substrate was precured at 210 °C in a N_2 atmosphere. The BCB thickness was reduced from the thickness of 6 μm in previous devices.[24] Then, the laser wafer and InP host substrate were bonded at 130 °C at a pressure of approximately 25 kPa followed by hard curing at 250 °C for 60 min in a N_2 atmosphere [Fig. 3-4)]. We used the n-InP host substrate for easy cleaving in this work, while we target membrane lasers bonded on silicon LSI circuits in the future. After that, the InP substrate side and GaInAs etch-stop layer (300-nm-thick) were removed by polishing and wet etching [Fig. 3-5)]. Finally, the Be-doped contact layer, except the p-electrode region, was removed, and Ti/Au electrodes were evaporated onto both p-contact and n-InP layers [Fig. 3-6)].

Figure 4 shows a cross-sectional scanning electron microscope (SEM) image of the fabricated LCI membrane FP laser with a stripe width W_s of approximately 1 μm. As can be seen, the distance between the stripe edges to the Ti/Au electrode was approximately 3 μm for both the p-InP and n-InP sides.

3. Experimental results

Figure 5 shows the typical light-output–current (P–I) and voltage–current (V–I) characteristics of the fabricated LCI membrane FP laser with a core thickness of 220 nm used in thermal analysis.[25] The stripe width and cavity length of the device were $W_s = 1$ μm and $L = 700$ μm, respectively. As can be seen from the P–I characteristic, a threshold current of 3.5 mA (threshold current density of 500 A/cm^2 for the 5QW active region) and an external differential quantum efficiency of 11%/facet were obtained under RT-CW conditions. From the V–I characteristic, we can confirm that the turn-on voltage, threshold voltage, and device resistance near the threshold are 0.8 V, 1.2 V, and 110 Ω, respectively. The device resistance is considerably high for the device size because the thickness of the p-InP cladding is only 220 nm, and the distance from the Ti/Au electrode to the active region is approximately 3 μm. These values are approximately 10 times and two times larger than those of con-

© 2015 The Japan Society of Applied Physics

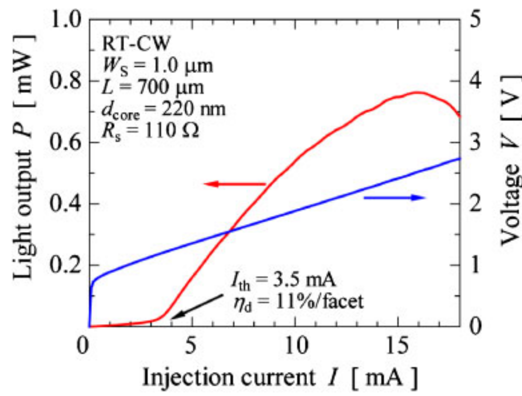

Fig. 5. (Color online) *P–I* and *V–I* characteristics of the fabricated LCI membrane FP laser.

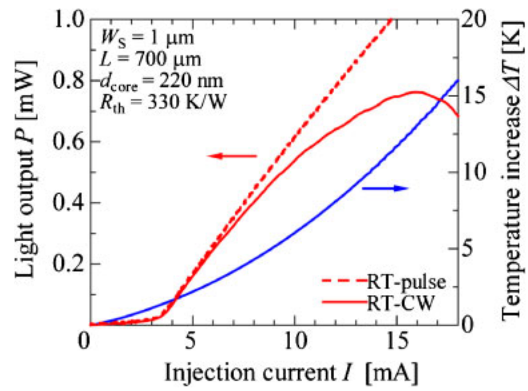

Fig. 7. (Color online) *P–I* characteristics of the fabricated LCI-membrane laser under CW and pulsed operation and the temperature increase as a function of the injection current.

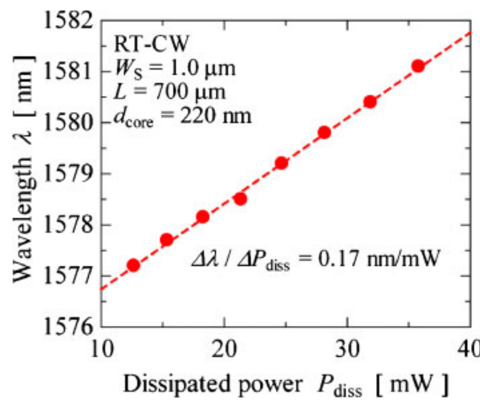

Fig. 6. (Color online) Peak wavelength of the gain as a function of the dissipated power of the LCI-membrane laser.

ventional vertical-injection-type buried-heterostructure (BH) lasers. For the realization of ultralow power-consumption operation of a membrane laser, a further reduction in the device resistance will be required because the ratio of the power consumption to the resistance increases drastically for very short-cavity DFB lasers with a strongly index-coupled grating structure.

The reason for the realization of RT-CW operation is attributed to the reduction in the thermal resistance by using a thinner BCB layer. In order to explain this, we also evaluated the peak lasing wavelength as a function of the dissipated power, as shown in Fig. 6. The dissipated power is given by the following relation:

$$P_{\mathrm{diss}} = V_{\mathrm{bias}} I_{\mathrm{bias}} - P_{\mathrm{o}}, \tag{1}$$

where V_{bias} is bias voltage, I_{bias} is bias current, and P_{o} is the output power of the laser. As can be seen from the fitting line in Fig. 6, the change in the lasing wavelength with respect to the change in the dissipated power, $\Delta\lambda/\Delta P_{\mathrm{diss}}$, was 0.17 nm/mW. From this result, the thermal resistance was estimated to be 330 K/W by assuming a typical value for $\Delta\lambda/\Delta T$ of 0.5 nm/K for GaInAsP/InP FP lasers emitting at a 1.5-µm wavelength.[26] This peak wavelength shift by increasing temperature results from the refractive index change due to lattice expansion. By using this thermal resistance R_{th}, the temperature increase ΔT in the active region can be obtained by the following equation:

$$\Delta T = R_{\mathrm{th}} \Delta P_{\mathrm{diss}}. \tag{2}$$

Figure 7 shows *P–I* characteristics for both CW and pulsed conditions and ΔT calculated from Eq. (2). It was found that the light output under CW conditions exhibited a roll-off tendency from the pulsed conditions due to a self-heating effect, and a roll-over was observed at an injection current of 16 mA, where the temperature increase was estimated to be 13 K, in contrast to only 1.4 K at the threshold.

4. Analysis of the thermal properties

In the previous section, the thermal resistance of the membrane laser was estimated from the experimental results. In this section, an analysis of the thermal properties by using a two-dimensional (2D) finite element method (FEM) is carried out, and its influence on a very short-cavity membrane DFB laser with low-power consumption operation is discussed. In the simulation model, the membrane laser is assumed to be on a Cu heat sink (width of 11 mm and height of 2 mm) with a 2-µm-thick air gap between the laser and the heat sink, which represents the roughness between the InP substrate and the Cu heat sink. Figure 8(a) shows the laser part of the simulation model. In the simulation, the 5QW active region was regarded as a bulk structure by using the average thermal conductivities of the quantum wells. We used the typical steady-state heat transfer equation[27]

$$-\nabla \cdot (\kappa_{\mathrm{T}} \nabla T) = Q, \tag{3}$$

where Q is the heat source density, κ_{T} is the thermal conductivity, and T is the temperature. The thermal conductivities used in the analysis[28–30] are listed in Table I. The boundary conditions are given by

$$T|_{\mathrm{sink}} = T_{\mathrm{s}} = 293\,\mathrm{K}, \tag{4}$$

$$\kappa_{\mathrm{T}} \nabla T = h(T - T_{\mathrm{s}}), \tag{5}$$

where T_{s} is the temperature at the bottom of the heat sink, and h is the heat transfer coefficient. In this simulation, h was assumed to be the typical value of $4.6\,\mathrm{W/(K \cdot m^2)}$ for nonconvective air, and we consider the recombination and absorption heat as well as the Joule heat in the active and p-InP regions as the total dissipated power. For a dissipated power of 11.3 mW (which corresponds to a bias current I_{bias} of 7 mA with a device resistance of 110 Ω), the dissipated powers in the active region and p-InP layer are 5.2 and 6.1 mW, respectively.

© 2015 The Japan Society of Applied Physics

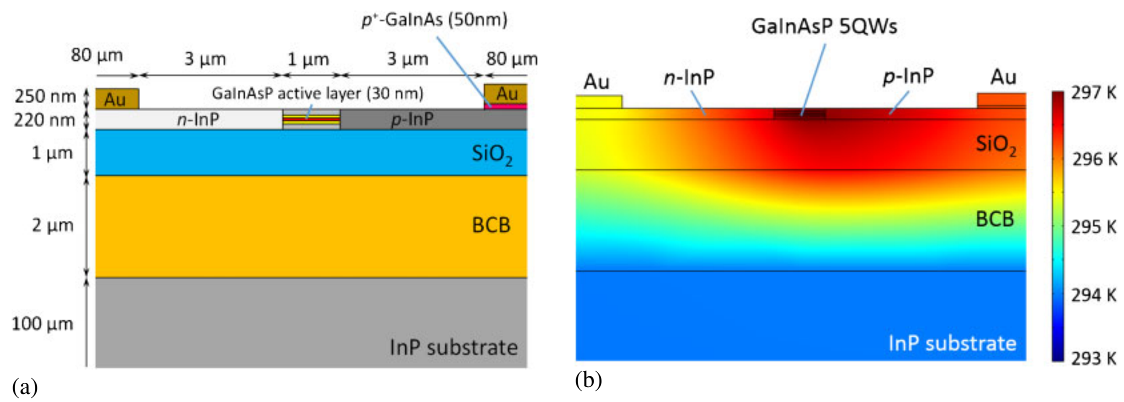

Fig. 8. (Color online) (a) Simulation model for thermal analysis. (b) Temperature distribution of the membrane structure using a 2D FEM with a dissipated power of 11.3 mW.

Table I. Thermal conductivity [W/(K·m)] for thermal analysis.[28–30]

Material	Thermal conductivity
Cu	400
Au	320
InP	68
$Ga_{0.22}In_{0.78}As_{0.81}P_{0.19}$ (well)	5.1
$Ga_{0.26}In_{0.74}As_{0.49}P_{0.51}$ (barrier)	5.2
$Ga_{0.47}In_{0.53}As$ (contact layer)	4.4
SiO_2	1.4
BCB	0.29

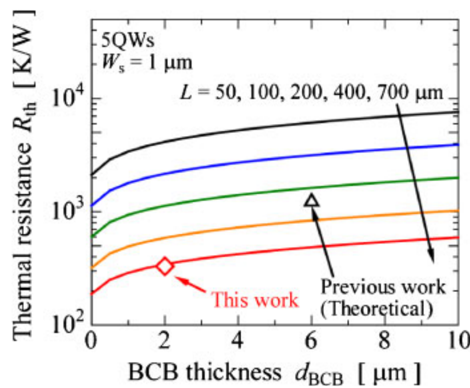

Fig. 9. (Color online) Calculated thermal resistance dependence on the BCB thickness for various structures.

Figure 8(b) shows the temperature distribution in the membrane structure calculated by the 2D FEM at a dissipated power of 11.3 mW (I_{bias} = 7 mA). The maximum temperature and the temperature increase in the active region are 296.9 and 3.9 K, respectively. As a result, a thermal resistance of 340 K/W was obtained, which is very close to the value of 330 K/W estimated from the experimental results of the lasing wavelength change versus the dissipated power.

Then, the thermal resistance dependence on the BCB thickness is calculated for various cavity lengths, as shown in Fig. 9, where the stripe width is kept constant at W_S = 1 μm. The measured thermal resistance in this work and that of the previous work[24] (calculated value) are also plotted in the same graph. As can be seen, the reduction in the BCB

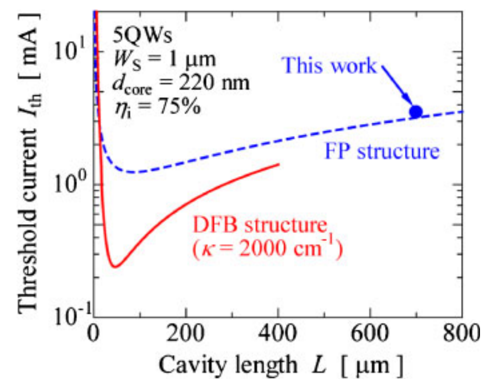

Fig. 10. (Color online) Calculated threshold-current dependence on the cavity length of the LCI membrane laser.

thickness from 6 to 2 μm enables a reduction in the thermal resistance by approximately 30%. Furthermore, the thermal resistance tends to increase owing to the increase in the device resistance for a shorter cavity. However, this heating problem will not be a serious problem when a short-cavity DFB structure is adopted, and the bias current is very low (approximately 1 mA) for the required output power of −8 dBm, which satisfies the requirements for on-chip optical interconnects.[30] From these results, it is determined that a relatively large thermal resistance has little influence on the laser operation for on-chip light sources.

Finally, we calculated the cavity-length dependence of the threshold current for LCI membrane lasers. Figure 10 shows these dependencies for an LCI membrane FP laser (solid line) and a DFB laser (dashed line) with an index-coupling coefficient $\kappa = 2000\,\mathrm{cm}^{-1}$, where the stripe width and the internal quantum efficiency were assumed to be 1 μm and 75%, respectively. The facet reflectivity of this membrane FP structure was calculated to be 20%.[25] As can be seen, the experimentally obtained threshold current (I_{th} = 3.5 mA, L = 700 μm) was close to theoretical one (I_{th} = 3.2 mA), and it can be reduced to 1 mA by shortening the cavity length to approximately 100 μm. The solid line in Fig. 10 indicates the threshold current for a DFB structure with $\kappa = 2000\,\mathrm{cm}^{-1}$ without facet reflection, which can be obtained by adopting a 40-nm-deep surface grating on the top InP layer. In this case, we calculated the threshold current in the cavity length

© 2015 The Japan Society of Applied Physics

of up to 400 μm because the external differential quantum efficiency is approximately zero at this cavity length. A threshold current of 0.24 mA can be attained for a cavity length of 46 μm. In this case, self-heating is approximately 8 K, which is negligible owing to the low operation current of approximately 1 mA, as mentioned before.

5. Conclusion

In conclusion, we experimentally and theoretically evaluated thermal properties of LCI membrane FP laser under a RT-CW operation. A threshold current of 3.5 mA, which corresponds to a threshold current density of 500 A/cm^2 for a 5QW active region, and an external differential quantum efficiency of 11%/facet were obtained for a stripe width of 1 μm and a cavity length of 700 μm. From the measurement, the experimental thermal resistance of 340 K/W, which is close to the simulated thermal resistance of 330 K/W, were obtained. This result shows that a suitable model for real devices was formulated. Using the developed simulation model, we showed that the reduction of BCB thickness is effective for the reduction of thermal resistance. Further, the possibility of low self-heating operation in extremely low-threshold-current DFB lasers by introducing a strongly index-coupled structure with short cavity was also presented.

Acknowledgment

This work was supported by JSPS KAKENHI Grant Numbers 24246061, 25709026, 25420321, and 13J08092.

1) D. A. B. Miller, Proc. IEEE **88**, 728 (2000).
2) P. Kapur, J. P. McVittie, and K. C. Saraswat, IEEE Trans. Electron Devices **49**, 590 (2002).
3) P. Kapur, G. Chandra, J. P. McVittie, and K. C. Saraswat, Trans. Electron Devices **49**, 598 (2002).
4) G. Chen, H. Chen, M. Haurylau, N. A. Nelson, D. H. Albonesi, P. M. Fauchet, and E. G. Friedman, Integration: VLSI J. **40**, 434 (2006).
5) K. Ohashi, K. Nishi, T. Shimizu, M. Nakada, J. Fujikata, J. Ushida, S. Torii, K. Nose, M. Mizuno, H. Yukawa, M. Kinoshita, N. Suzuki, A. Gomyo, T. Ishi, D. Okamoto, K. Furue, T. Ueno, T. Tsuchizawa, T. Watanabe, K. Yamada, S. Itabashi, and J. Akedo, Proc. IEEE **97**, 1186 (2009).
6) R. H. Dennard, F. H. Gaensslen, V. L. Rideout, E. Bassous, and A. R. Leblanc, IEEE J. Solid-State Circuits **9**, 256 (1974).
7) D. A. B. Miller, Proc. IEEE **97**, 1166 (2009).
8) P. Moser, W. Hofmann, P. Wolf, J. A. Lott, G. Larisch, A. Payusov, N. N. Ledentsov, and D. Bimberg, Appl. Phys. Lett. **98**, 231106 (2011).
9) S. Imai, K. Takaki, S. Kamiya, H. Shimizu, J. Yoshida, Y. Kawakita, T. Takagi, K. Hiraiwa, H. Shimizu, T. Suzuki, N. Iwai, T. Ishikawa, N. Tsukiji, and A. Kasukawa, IEEE J. Sel. Top. Quantum Electron. **17**, 1614 (2011).
10) A. Kasukawa, IEEE Photonics J. **4**, 642 (2012).
11) P. Wolf, P. Moser, G. Larisch, W. Hofmann, and D. Bimberg, IEEE J. Sel. Top. Quantum Electron. **19**, 1701207 (2013).
12) M. Fujita, R. Ushigome, and T. Baba, Electron. Lett. **36**, 790 (2000).
13) J. V. Campenhout, P. Rojo-Romeo, P. Regreny, C. Seassal, D. V. Thourhout, S. Verstuyft, L. D. Cioccio, J.-M. Fedeli, C. Lagahe, and R. Beaets, Opt. Express **15**, 6744 (2007).
14) B. Ellis, M. A. Mayer, G. Shambat, T. Sarmiento, J. Harris, E. E. Haller, and J. Vučković, Nat. Photonics **5**, 297 (2011).
15) S. Matsuo, T. Sato, K. Takeda, A. Shinya, K. Nozaki, H. Taniyama, M. Notomi, K. Hasebe, and T. Kakitsuka, IEEE J. Sel. Top. Quantum Electron. **19**, 4900311 (2013).
16) K. Takeda, T. Sato, A. Shinya, K. Nozaki, W. Kobayashi, H. Taniyama, M. Notomi, K. Hasebe, T. Kakitsuka, and S. Matsuo, Nat. Photonics **7**, 569 (2013).
17) T. Okamoto, N. Nunoya, Y. Onodera, S. Tamura, and S. Arai, Electron. Lett. **38**, 1444 (2002).
18) T. Okamoto, N. Nunoya, Y. Onodera, T. Yamazaki, S. Tamura, and S. Arai, IEEE J. Sel. Top. Quantum Electron. **9**, 1361 (2003).
19) S. Sakamoto, H. Naitoh, M. Otake, Y. Nishimoto, S. Tamura, T. Maruyama, N. Nishiyama, and S. Arai, IEEE J. Sel. Top. Quantum Electron. **13**, 1135 (2007).
20) S. Sakamoto, H. Naitoh, M. Ohtake, Y. Nishimoto, T. Maruyama, N. Nishiyama, and S. Arai, Jpn. J. Appl. Phys. **46**, L1155 (2007).
21) K. Oe, Y. Noguchi, and C. Caneau, IEEE Photonics Technol. Lett. **6**, 479 (1994).
22) T. Okumura, M. Kurokawa, M. Shirao, D. Kondo, H. Ito, N. Nishiyama, T. Maruyama, and S. Arai, Opt. Express **17**, 12564 (2009).
23) T. Shindo, M. Futami, T. Okumura, R. Osabe, T. Koguchi, T. Amemiya, N. Nishiyama, and S. Arai, 16th Opto-Electronics and Communications Conf. (OECC2011), 2011, 6D3_7.
24) M. Futami, T. Shindo, K. Doi, T. Amemiya, N. Nishiyama, and S. Arai, 24th Int. Conf. on Indium Phosphide and Related Materials (IPRM 2012), 2012, p. 285.
25) K. Doi, T. Shindo, M. Futami, J. Lee, T. Hiratani, D. Inoue, S. Yang, T. Amemiya, N. Nishiyama, and S. Arai, 25th Int. Conf. Indium Phosphide and Related Materials (IPRM 2013), 2013, Wed2-3.
26) S. Arai, Y. Suematsu, and Y. Itaya, IEEE J. Quantum Electron. **16**, 197 (1980).
27) H. K. Lee, Y. M. Song, Y. T. Lee, and J. S. Yu, Solid-State Electron. **53**, 1086 (2009).
28) W. Nakwaski, J. Appl. Phys. **64**, 159 (1988).
29) G. Hatakoshi, M. Onomura, M. Yamamoto, S. Nunoue, K. Itaya, and M. Ishikawa, Jpn. J. Appl. Phys. **38**, 2764 (1999).
30) K. Doi, T. Shindo, J. Lee, T. Amemiya, N. Nishiyama, and S. Arai, IEEE J. Quantum Electron. **50**, 321 (2014).

© 2015 The Japan Society of Applied Physics